applied sciences

MDPI

Article

Mechanical Feasibility of Asphalt Materials for Pavement Solar Collectors: Small-Scale Laboratory Characterization

Marco Pasetto, Andrea Baliello, Giovanni Giacomello and Emiliano Pasquini *

Department of Civil, Environmental and Architectural Engineering, University of Padova, Via Marzolo 9, 35131 Padova, Italy
* Correspondence: emiliano.pasquini@unipd.it

Abstract: Rutting (i.e., depressions along the wheel path) is a distress exhibited by flexible asphalt pavements at high in-service temperatures negatively affecting ride comfort and safety. In this regard, the fine asphalt mortar (i.e., bitumen filler and fine sand) plays a key role in the rutting potential of the asphalt mixtures. Given this background, this manuscript presents a small-scale laboratory experimentation aimed at assessing the rutting-related performance of a plain bitumen combined with natural (limestone) or manufactured (steel slag) fine aggregates (size up to 0.18 mm) through advanced experimental and theoretical approaches. Specific rheological tests through dynamic shear were carried out to achieve this goal. The investigated asphalt blends came from a wider research project focused on the implementation of a pavement solar collector (a road system to harvest the solar energy irradiating the pavement). In particular, the present paper aimed at verifying the mechanical suitability of the produced asphalt mixes with respect to permanent deformation resistance. Such a small-scale investigation mainly showed that the previously selected constituent materials did not imply criticisms in terms of rutting response.

Keywords: road pavement; asphalt; binder; mastic; fine mortar; rutting; permanent deformation; fractional model; rheology; solar collector

Citation: Pasetto, M.; Baliello, A.; Giacomello, G.; Pasquini, E. Mechanical Feasibility of Asphalt Materials for Pavement Solar Collectors: Small-Scale Laboratory Characterization. *Appl. Sci.* **2023**, *13*, 358. https://doi.org/10.3390/app13010358

Academic Editors: Cesare Oliviero Rossi, Pietro Calandra, Paolino Caputo, Bagdat Teltayev, Valeria Loise and Michele Porto

Received: 29 November 2022
Revised: 20 December 2022
Accepted: 22 December 2022
Published: 27 December 2022

1. Introduction

Rutting on road pavements is a common distress occurring at high in-service temperature and consists of depressions of the surface asphalt layer(s) along the wheel path [1] leading to lower ride quality and safety and, thus, higher maintenance costs [2–4].

From the physical point of view, rutting is generated by different sub-phenomena. First, some early densification can occur after the opening to traffic. Such an early-stage phenomenon is mainly related to the mix's lithic skeleton [5] and can be also ascribed to working loads, in particular for high-void bituminous mixes [6]. Moreover, a long-term development of rutting is due to the shear-related deformations of the asphalt mixtures which lead to visible lateral plastic flows in the proximity of the rut depressions [7–9]. A further contribution could arise from local volume increase in the upheaval zone, where local high-void contents can be detected [10]. Finally, the loss of materials due to raveling along the rutted wheel paths can contribute, even if it is usually negligible with respect to other contributions [11].

Thus, rutting can be associated with both inadequate bituminous mortar consistency and aggregate skeleton structure. However, since the role of asphalt phase is generally predominant with respect to that of aggregate gradation [12], the most relevant factor involved in the study of rutting phenomena is typically related to the temperature-dependent visco-elastic response of the bituminous phase [13], which affects the overall permanent deformation resistance of the asphalt mixture [14].

In this regard, besides traditional basic indicators of bitumen behavior (viscosity, softening point, etc.), more advanced parameters and methodologies are suggested to

analyze permanent deformation resistance of asphalt binders such as, for example, $G^*/sin\delta$, where G^* is the norm of the complex shear modulus and δ is the corresponding phase angle determined in the linear visco-elastic domain [15], as well as multiple stress creep-recovery tests carried out in rotational (shear) configuration [16]. Moreover, various analytical and physical models were developed/adapted to mathematically describe the rutting behavior of asphalt pavements. As an example, a simple visco-elastic (Kelvin-Voigt) model was used to analyze the binder shear resistance with respect to rutting [17] along with other analytical tools [18], regression models and neural networks [19], or three-dimensional finite element methods [20].

2. Research Goals and Approach

Given this background, this paper presents an experimental study aimed at evaluating the rutting potential of different asphalt blends. In particular, the study is addressed to the small-case analysis of such blends since, according to literature [21,22], mastic and mortar phases of bituminous mixtures have a crucial influence on the mechanical performance of asphalt mixtures [23]. In this regard, several researchers report that small-scale samples including fine aggregate particles could reliably reflect the physical-chemical interactions between the asphalt binder and the aggregates [24].

Starting from this assumption, this research study evaluates specific rutting-related features at such a scale of analysis, investigating special constituent materials composing the asphalt blends. In fact, the study builds upon a previous step of a wider research project which investigated the thermal efficiency of a road energy harvesting system constituted by a steel-pipe-based asphalt solar collector (ASC) and various asphalt mixes [25]. In such a study [25], special constituent materials and mix-design proportions were selected for thermal purposes mainly. The peculiar characteristics of the ASC were (Figure 1):

- thanks to its conduction properties, a manufactured steel slag aggregate was included in the lithic skeleton (composed by natural limestone aggregate) in order to enhance the thermal conduction within the asphalt layer, and the related solar collector efficiency [26];
- a rather fine aggregate gradation (with nominal maximum aggregate size of 8 mm) was designed to make the mixture structure compatible with the presence of the collector without compromising the functionality of the 4 cm thick covering asphalt layer;
- a low target air-void content was selected for enhancing the thermal transmission within the asphalt layer, since air voids can act as insulators.

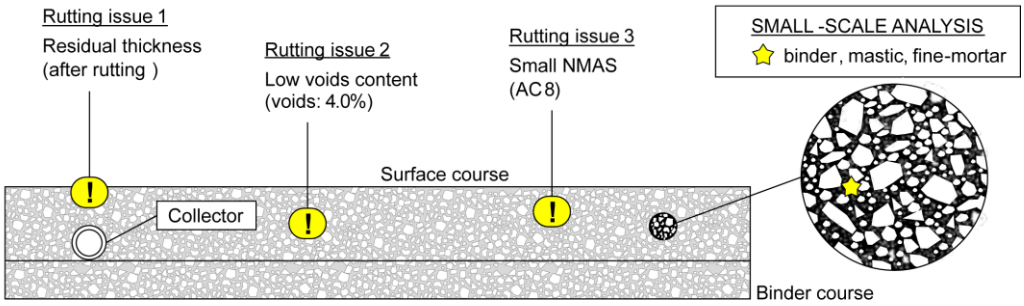

Figure 1. Background from the previous research [25].

The above characteristics allowed an efficient energy collection, effectively converting the solar radiation to thermal energy, but they can lead to unacceptable rutting potential. Therefore, the present paper reports the high-temperature mechanical properties of the fine mortar phase of the abovementioned asphalt mixes produced with energy harvesting purposes.

Overall, such a research study can enhance the knowledge in the field since it is specifically addressed towards the study of unconventional materials (i.e., materials containing steel slag aggregates and characterized by special proportions of constituents) through the use of quite common testing methodologies, applied at unconventional scale (i.e., fine mortar scale) and using unconventional methods of data analysis.

In particular, the rutting performance at bitumen-, mastic-, and fine-mortar scale was analyzed both using conventional (limestone) or steel slag aggregates and a plain (non-modified) bitumen according to the original mix design for the asphalt layer of the solar collector [25]. The Dynamic Shear Rheometer (DSR) was used to accomplish the objective by testing the asphalt binder, mastics (bitumen + filler with size < 0.075 mm), and fine mortars (bitumen + filler + fine aggregates with size up to 0.18 mm), reproducing the constituent proportions of the original bituminous mixtures [25]. Such a testing approach could be considered quite innovative, since few studies exist on the use of DSR for studying the asphalt blends at fine-mortar scale [27].

After a preliminary characterization of the physical properties of the binder and the fine aggregates, several rheological tests were performed analyzing the Linear Visco-Elastic (LVE) properties and the rutting performance of the materials. Binder, mastics, and fine mortars were tested after short-term laboratory aging (Rollin Thin Film Oven—RTFO—test according to EN 12607-1) to simulate the real in-service conditions after material's production and paving. The experimental plan is summarized in Figure 2 (the codes in the flowchart are specified in the following paragraphs).

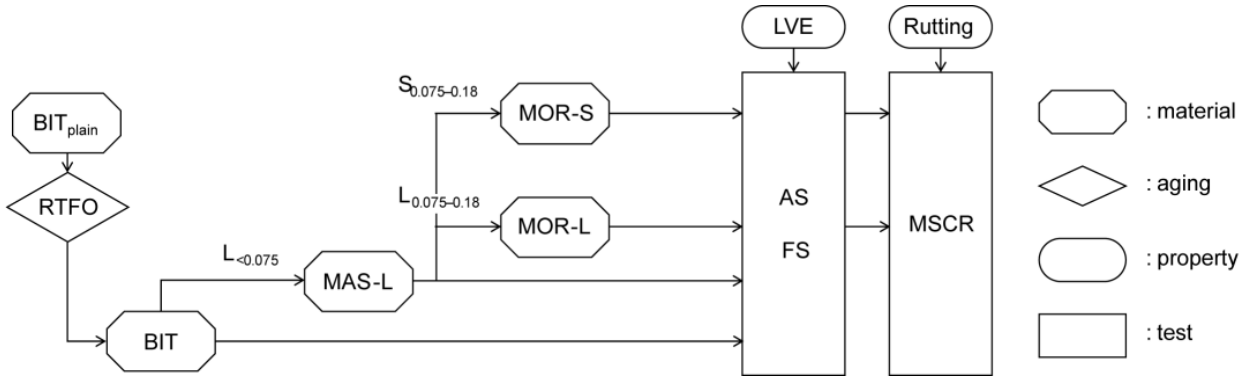

Figure 2. Schematization of the experimental plan.

3. Materials and Methods

3.1. Constituent Materials

As anticipated, constituent materials were selected in order to reproduce the previously studied asphalt mixes [25]. A 50/70 penetration grade non-modified bitumen (coded as BIT_{plain}) was utilized as binder. Its basic characteristics are summarized in Table 1. Limestone (coded *L*) and electric-arc-furnace steel slag (coded *S*) fine aggregates were used; *L* represented a conventional reference natural material whereas *S* was a manufactured aggregate that could also be used for recycling purposes. Physical properties of the studied aggregates are reported in Table 2, whereas their morphological composition is given in Table 3.

Table 1. Basic characteristics of the selected asphalt binder.

Characteristic	Test Method	Unit	Value
Penetration at 25 °C	EN 1426	0.1 mm	53
Softening point	EN 1427	°C	50.0
Retained pen. at 25 °C after RTFO	EN 1426	%	70
Increase in soft. point after RTFO	EN 1427	°C	6.6
Ductility at 25 °C	ASTM D113	cm	>100

Table 2. Physical properties of the selected aggregates.

Characteristic	Test Method	Unit	Value	
			Limestone	Steel Slag
Particle density	EN 1097-6	Mg/m^3	2.76	3.84
Shape index	EN 933-4	%	12.8	7.8
Flakiness index	EN 933-3	%	10.5	8.3
Sand equivalent	EN 933-8	%	78	92
Rigden voids	EN 1097-4	%	32.7	–

Table 3. Morphological composition of the selected aggregates.

Aggregates	Oxide Content [%]							
	MgO	Al_2O_3	SiO_2	CaO	TiO_2	Cr_2O_3	MnO	FeO
L	2.50	1.00	3.34	52.71	–	–	–	0.39
S	3.65	9.30	13.02	29.60	0.35	4.03	5.09	32.84

Mastics (bitumen + filler with size < 0.075 mm) and fine mortars (bitumen + filler + fine aggregates with size up to 0.18 mm) were prepared combining the different components in order to comply with the previous mix designs [25]; in particular, a single mastic (coded *MAS-L*) was prepared with the 50/70 pen bitumen and the *L* filler using a bitumen to filler ratio of 100:130 by weight. Steel slag mastic was not produced because only limestone filler was used in the original study.

Then, two different fine mortars (characterized by aggregate size < 0.18 mm) were prepared blending the bitumen, the *L* filler and the *L* or *S* fine fraction (i.e., fine aggregates having particle size between 0.075 and 0.18 mm); such fine mortars were coded as *MOR-L* (bitumen, *L* filler and *L* fine fraction with a ratio of 100:130:95 by weight, respectively) and *MOR-S* (bitumen, *L* filler, and *S* fine fraction with a ratio 100:130:132 by weight, respectively); taking into account the different particle density of the different aggregates, the two mortars were characterized by the same volumetric proportions of constituents.

3.2. Samples Preparation

Bitumen BIT_{plain} was initially subjected to a laboratory short-term aging (through RTFO test) to reproduce the real service conditions with the highest rutting potential. For the sake of brevity, the short-term aged bitumen is coded as *BIT*.

In the case of *MAS-L*, the short-term aged bitumen was blended at 160 °C with the *L* filler through an automatic stirring equipment (30 min stirring to ensure adequate homogeneity) according to the dosage mentioned above.

A similar procedure was followed to prepare the mortars (*MOR-L* or *MOR-S*); here, the *BIT* was mixed with the selected fillers (particle size < 0.075 mm) and fine sand fractions *L* or *S* (0.075 mm < size < 0.18 mm) using the same stirring procedure.

Then, cylindrical samples for binder testing were produced, pouring the hot bituminous blends in specific silicon molds (8-mm diameter 2-mm thick, or 25-mm diameter 1-mm tick). After production, specimens were stored at room temperature for at least one day before testing.

3.3. Testing Methods

Bitumen *BIT* (in RTFO-aged condition) was studied by performing different tests with the DSR (EN 14770) in order to assess the rheological response of the binder within the typical in-service temperature range.

First, oscillatory Amplitude Sweep (AS) tests were carried out with a parallel plate geometry to identify the LVE domain, i.e., the strain domain where the response is linear with respect to the stress/strain level applied [28]. Using the 8 mm diameter *BIT* samples (with testing gap of 2 mm), three test replicates were executed, increasing the shear strain γ from 0.01 to 100% (through logarithmic ramps) at a test frequency f of 20 Hz. Tests were

carried out at a temperature T of 10 °C (a pre-conditioning time of 15 min was established to ensure the thermal homogeneity on samples). At such testing conditions, the lowest LVE limit was found and then applied for all the following rheological tests carried out at higher temperatures and/or lower frequencies [29]. The complex shear modulus G^* and the related phase angle δ (i.e., the delay of the response due to the visco-elastic nature of the binder/blends) were measured, allowing calculation of G' (storage modulus) and G'' (loss modulus). According to wide literature, LVE limits were identified as the strain level corresponding to a G^* decreased to 95% of its initial value [30].

Frequency Sweep (FS) oscillatory tests were then carried out in parallel plate geometry using a strain level within the LVE domain; a test frequency varying from 0.1 to 20 Hz was selected. Such frequency sweeps were carried out at temperatures ranging from 10 to 80 °C, with step of 10 °C using a pre-conditioning time of 15 min at each T; 8 mm diameter samples (with testing gap of 2 mm) or 25 mm diameter samples (with gap of 1 mm) were tested; the geometric test configuration was selected based on expected stiffness of the tested sample (two replicates for each test). Experimental data were first represented in Black diagrams (phase angle δ vs. norm of complex modulus G^*) to check the alignment of the experimental data series in a unique curve (this happens for thermorheological simple materials), and thus to verify the consistency of the well-known Williams–Landel–Ferry equation [31] and the related time–temperature superposition principle. Based on FS results for *BIT*, preliminary basic information about its rutting potential were evinced; this was accomplished by calculating the $G^*/sin\delta$ parameter at 10 rad/s (1.59 Hz) as suggested by the Performance Grade (PG) classification approach [32].

Then, the responses of the binder were finally evaluated in terms of rutting potential considering the high in-service temperatures to which the bitumen will be subjected. This was accomplished through Multiple Stress Creep Recovery (MSCR) tests (EN 16659) on 25 mm diameter samples (parallel plate DSR geometry—testing gap 1 mm). Three test replicates for each material and four test temperatures (50, 60, 70, and 80 °C) were analyzed. A pre-conditioning time of 15 min at the testing temperature was again selected. For *BIT*, the test protocol consisted of the application of consecutive creep-recovery cycles under different stress levels τ (0.1 and 3.2 kPa); in particular, 10 cycles constituted by 1.0 s of creep loading and 9.0 s of rest period were repeated for each of the two stress levels on the same sample. Binder performance was assessed by averaging the results of the three test replicates. At a generic nth cycle, ${\varepsilon^n}_0$ is the deformation at the beginning of creep load application, ${\varepsilon^n}_1$ is the strain after the creep phase of 1.0 s, and ${\varepsilon^n}_{10}$ is the final strain at the end of the given cycle. Then, the ${R_\%}^\tau$ parameter was used to express the average recovery aptitude of the material for the selected stress level τ (average of 10 cycles) according to Equation (1):

$$\sum_{n=1}^{10} {R_\%}^\tau = 100\ ({\varepsilon^n}_1 - {\varepsilon^n}_0)/{\varepsilon^n}_1 \quad (1)$$

The non-recoverable creep compliance ${J_{nr}}^\tau$ can be calculated as reported in Equation (2):

$$\sum_{n=1}^{10} {J_{nr}}^\tau = {\varepsilon^n}_{10}/\tau \quad (2)$$

Analogously, the ${J_{nr}/J_{tot}}^\tau$ ratio illustrated in Equation (3) represent the ratio between the compliance referring to the non-recoverable strain at the end of the cycle and the compliance referring to the maximum strain measured ate the end of the creep phase:

$$\sum_{n=1}^{10} {J_{nr}/J_{tot}}^\tau = [({\varepsilon^n}_r - {\varepsilon^n}_0)/\tau]/[({\varepsilon^n}_c - {\varepsilon^n}_0)/\tau] = ({\varepsilon^n}_r - {\varepsilon^n}_0)/({\varepsilon^n}_c - {\varepsilon^n}_0) \quad (3)$$

where, ${\varepsilon^n}_r$ is the absolute strain value at the end of the cycle and ${\varepsilon^n}_c$ is the absolute strain value at the end of the creep phase.

As far as the mastic scale (binder + filler) and the mortar scale (binder + filler + fine sand) are concerned, *MAS-L*, *MOR-L*, and *MOR-S* were tested with the same AS, FS, and MSCR test protocols to identify their LVE properties and rutting potential, which will sensibly vary as a consequence of the stiffening effect due to the aggregates [33]. LVE strain limit resulting from AS was again used to carry out FS tests. In this case, MSCR tests were carried out at three consecutive stress levels τ (i.e., 0.1, 3.2, and 10 kPa) in order to achieve a more representative picture of the blends' performance testing stiffer materials with respect to bitumen.

3.4. MSCR Data Modelling

To better understand rutting potential at binder-, mastic-, and fine-mortar scales, a further elaboration of high-temperature experimental data collected through MSCR tests was then carried out. This allowed achievement of a more detailed description of the visco-elastic deformations exhibited by blends during each test cycle, thus differentiating eventual different behaviors of materials finally characterized by similar creep-recovery summary results (i.e., strain recoveries and compliances). To accomplish this objective, each cycle was modelled using an analytical approach able to model the whole creep-recovery curve of tested materials at each loading cycle [34]. The use and validation of such a model, originally validated for polymer- and rubber-modified asphalt binders at the mastics- and fine-mortar scale, for testing unconventional materials such as the steel-slag fine aggregates used for the solar collector asphalt layers is rather innovative.

Based on the abovementioned modelling approach, fractional calculus was used to fit the experimental results based on the rheological model schematized in Figure 3. In analogy with the work of Sapora et al. [34], a springpot and dashpot in series were considered to model the visco-elastic measured response. The first element (springpot) is obtained, replacing the first-order derivatives of generalized rheological models (e.g., Maxwell, Kelvin-Voigt models) with derivatives of order α [35]. Its constitutive relation is represented in Equation (4), where α ranges from 0 and 1. For $\alpha = 0$, the element turns in a spring, whereas a conventional dashpot is considered when $\alpha = 1$. Based on this hypothesis, parameter b_1 assumes a different physical meaning depending on α value (it stands for the element stiffness when $\alpha = 0$ or the viscosity when $\alpha = 1$). The second element (dashpot) was introduced to attain a residual permanent strain at the end of each test cycle (b_2 indicated its viscosity).

$$\sigma(t) = b_1 \frac{d^{\alpha}\varepsilon(t)}{dt^{\alpha}} \tag{4}$$

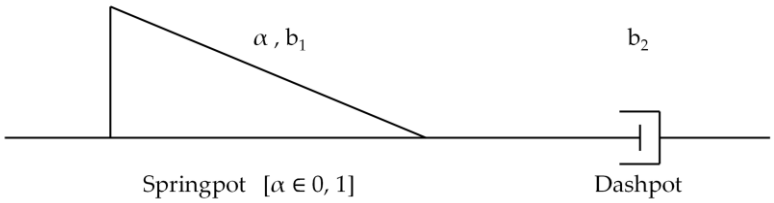

Figure 3. Creep-recovery proposed model: springpot in series with dashpot.

Under the proposed assumptions, the overall constitutive law of the model is given in Equation (5):

$$\varepsilon(t) = \left\{ \left[\frac{t^{\alpha}}{b_1\Gamma(1+\alpha)} + \frac{t}{b_2} \right] U(t) - \left[\frac{(t-t^*)^{\alpha}}{b_1\Gamma(1+\alpha)} + \frac{(t-t^*)}{b_2} \right] U(t-t^*) \right\} \sigma_0 \tag{5}$$

where, α, b_1, and b_2 are the already described parameters; σ_0 indicates the stress level applied to cycle, and t^* expresses the time at which unloading starts (1 s); Γ is the Euler-Gamma function; U is the unit step Heaviside function. Adopting such a mathematical approach, the use of complex power-laws commonly associated to the creep-loading

loading configuration of traditional rheological models was prevented, involving the fractional model with non-integer order derivatives. Additional details about the proposed model can be found elsewhere [34–36].

4. Experimental Results

First, the experimental results of preliminary AS tests (10 °C, 20 Hz) on binder-, mastic-, and fine-mortar are depicted in Figure 4a, and allow identification of the LVE limits used for FS analysis. Such LVE limits (calculated as average of the three test replicates) were equal to 0.40%, 0.20%, 0.08%, and 0.07% for *BIT*, *MAS-L*, *MOR-L*, and *MOR-S*, respectively. The results measured for *BIT* were in accordance with those commonly found for a non-polymer-modified bitumen for road applications. As expected, the progressive inclusion of lithic fractions (passing from binder to mastic and fine mortars) led to a clear stiffening effect that determined progressively reduced LVE domains. Comparing limestone- and steel-slag-based samples, no substantial differences in LVE limits were detected at this scale of analysis, notwithstanding an expected higher stiffness for *MOR-S*.

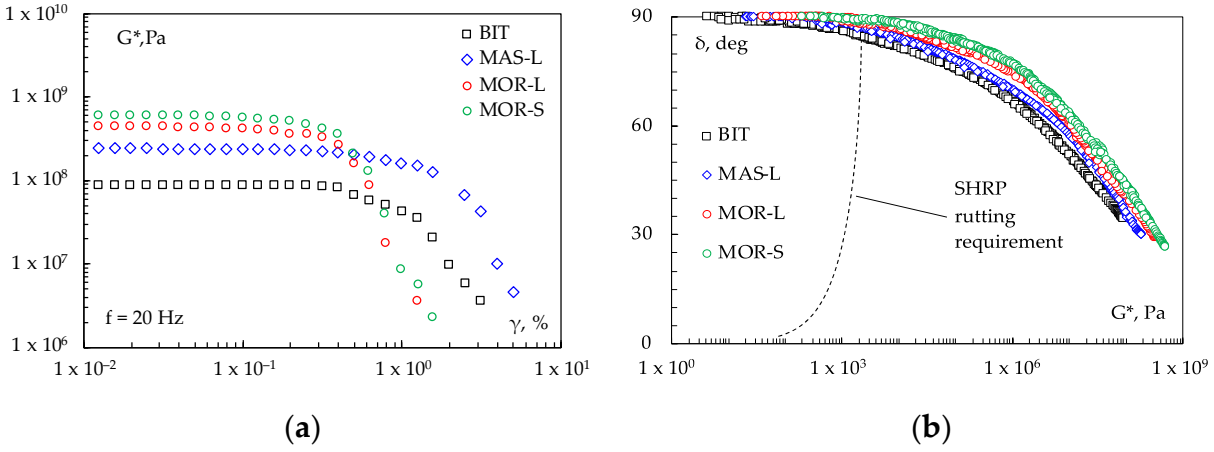

Figure 4. AS and FS results: G^* vs. γ for LVE limit study (**a**); Black diagrams δ vs. G^* (**b**).

Frequency sweep test results, achieved within the identified LVE domain, are presented in terms of phase angle and complex shear modulus in the Black space (Figure 4b). Again, the above-mentioned stiffening effect due to the addition of the mineral particles was clear. Higher stiffness of mastic- and fine-mortar samples was even more marked in the central part of the curves which refer to the intermediate and high in-service test temperatures (approximately between 30 and 60 °C). At higher temperatures (where rutting potential is higher), such a stiffening effect was still significant. Within the whole investigated domain, *MOR-S* showed higher stiffness with respect to the corresponding reference *MOR-L*. Moreover, this higher stiffness generally corresponded to a slightly lower elasticity of the material (higher phase angles δ). This suggested that the addition of manufactured steel-slag fine aggregates to the binder, rather than conventional limestone, can affect the bitumen-aggregate interaction, and thus the overall rheological response of the blends. Furthermore, the alignment of the data series in the Black space demonstrates the validity of the time–temperature superposition principle also at this scale. With respect to the $G^*/sin\delta$ parameter, the average values (three replicates) resulting from RTFO-aged bitumen analysis (Table 4) suggest a Performance Grade upper limit likely equal to 52 °C, which can be considered acceptable for a 50/70 penetration grade plain bitumen.

Table 4. RTFO-aged *BIT* $G^*/sin\delta$ values for PG upper temperature classification (1.59 Hz).

	Temperature [°C]											
	15	**20**	**25**	**30**	**35**	**40**	**45**	**50**	**55**	**60**	**75**	**80**
G^* [kPa]	10,573	3610	1092	300	79.83	23.30	7.46	3.10	1.22	0.68	0.30	0.12
Δ [deg]	51.37	59.18	66.33	72.20	76.46	79.80	82.43	84.51	86.02	87.00	88.24	88.50
$G^*/sin\delta$ [kPa] *	13,535	4204	1192	315	82.11	23.67	7.53	3.11	1.23	0.68	0.30	0.12

* SHRP requirement for upper PG temperature [32]: $G^*/sin\delta$ > 2.20 kPa.

As far as MSCR test results are concerned, the experimental findings in terms of percentage recovery $R_{\%}$, non-recoverable creep compliance J_{nr}, and non-recoverable creep compliance to total creep compliance J_{nr}/J_{tot} are depicted in Figure 5. For the sake of brevity, only the results obtained for the more critical applied stress levels τ (3.2 and 10 kPa) are plotted. As expected, the above-mentioned stiffness characteristics, hierarchically greater for *MOR-S*, *MOR-L*, and *MAS-L*, clearly reflect a gradually-increasing aptitude to recover deformations, even if at the higher tested temperatures (70 and 80 °C) such a strain-recovery ability significantly decreased.

Similar considerations can be drawn based on J_{nr} experimental findings. Overall, mastic and fine mortars showed a behavior not dependent on test temperature and stress level up to 70 °C. As far as the influence of steel slag (*MOR-S*) on the non-recoverable creep compliance is concerned, a higher anti-rutting effect with respect to the reference case (*MOR-L*) was clearly observed (lower strain accumulation). According to specific literature [37], such results are likely related to the higher stiffness in the case of steel slag blends with respect to the corresponding traditional limestone-based material. Thus, the corresponding steel-slag-based asphalt mixture can be supposed to be characterized by an overall reduced rutting potential, which is of crucial importance for preventing excessive permanent strain accumulation for the investigated solar collector at high in-service temperatures.

A more representative picture of the permanent deformation resistance of the studied blends is given by the J_{nr}/J_{tot} ratios. In this sense, it is worth noting that such parameters can vary from 0% (elastic material completely recovering the accumulated strain) to 100% (viscous material not recovering any accumulated strain). As expected, decreased J_{nr}/J_{tot} when temperature and stress level increased were observed. J_{nr}/J_{tot} approaching 100% were measured at temperatures higher than 70 °C, regardless of the stress level. However, this ratio was lower for *MOR-S* with respect to corresponding *MOR-L*, highlighting again the reduced rutting potential due to the adoption of steel slag aggregates. In this regard, it is worth noting that such behavior could be likely due to the superior characteristics of the manufactured aggregate (angularity, roughness, toughness, etc.) rather than to a different chemical interaction with the bitumen [38]. At any rate, such experimental findings cannot be ascribed to different constituent proportions, since the blends were designed to attain exactly the same volumetric proportion among the constituents, properly taking into account the different particle densities of the aggregates.

As anticipated, a complete description of the evolutive visco-elastic behavior during MSCR tests was attained through the application of the described fractional model. The three model parameters (α, b_1, b_2) introduced in Equation (5) were determined by a mathematical fitting procedure (i.e., the bisquare trust-region Matlab algorithm) of the creep-recovery curves over the different testing cycles. The fifth cycle for each τ-T combination and material was analyzed as a representative case, since negligible variations over the 10 cycles were recorded at the same τ-T.

Figure 6 presents an example of graphical model fitting for the recovery phases of the different materials at 60 °C and 0.1 kPa (experimental data and fitted model are given in the main y-axis, while residuals r are plotted in the secondary y-axis). All the model coefficients are then presented in the following Table 5, along with the fitting reliability (expressed as R-square—sum squared error—SSE); it can be noted that, overall, a very high

goodness of fit was also obtained (Table 5) in the case of unconventional mastic and fine mortar tested materials.

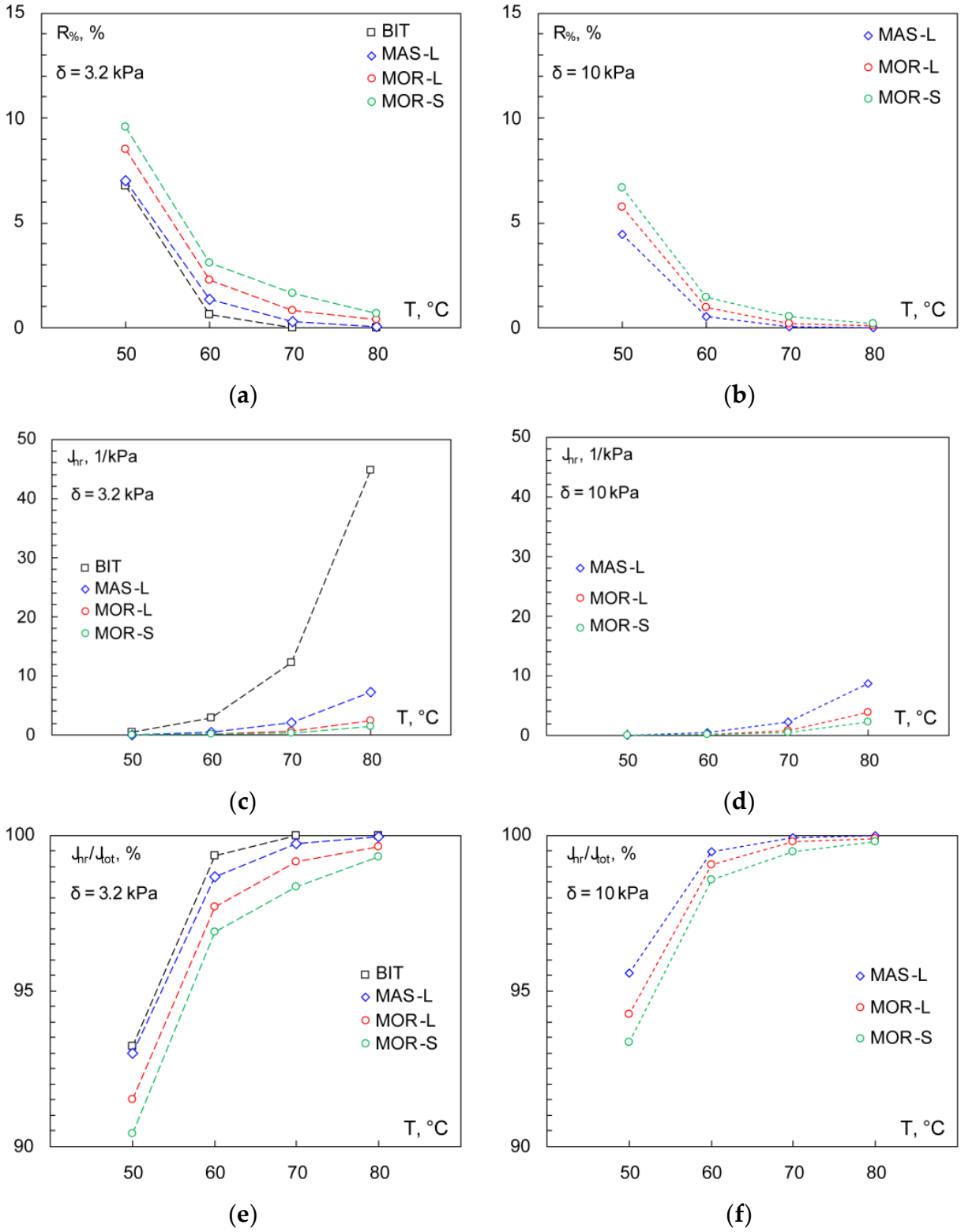

Figure 5. MSCR test results. Percentage recovery $R_{\%}$ at 3.2 (**a**) and 10 kPa (**b**); non-recoverable creep compliance J_{nr} at 3.2 (**c**) and 10 kPa (**d**); non-recoverable creep compliance related to total creep compliance J_{nr}/J_{tot} at 3.2 (**e**) and 10 kPa (**f**).

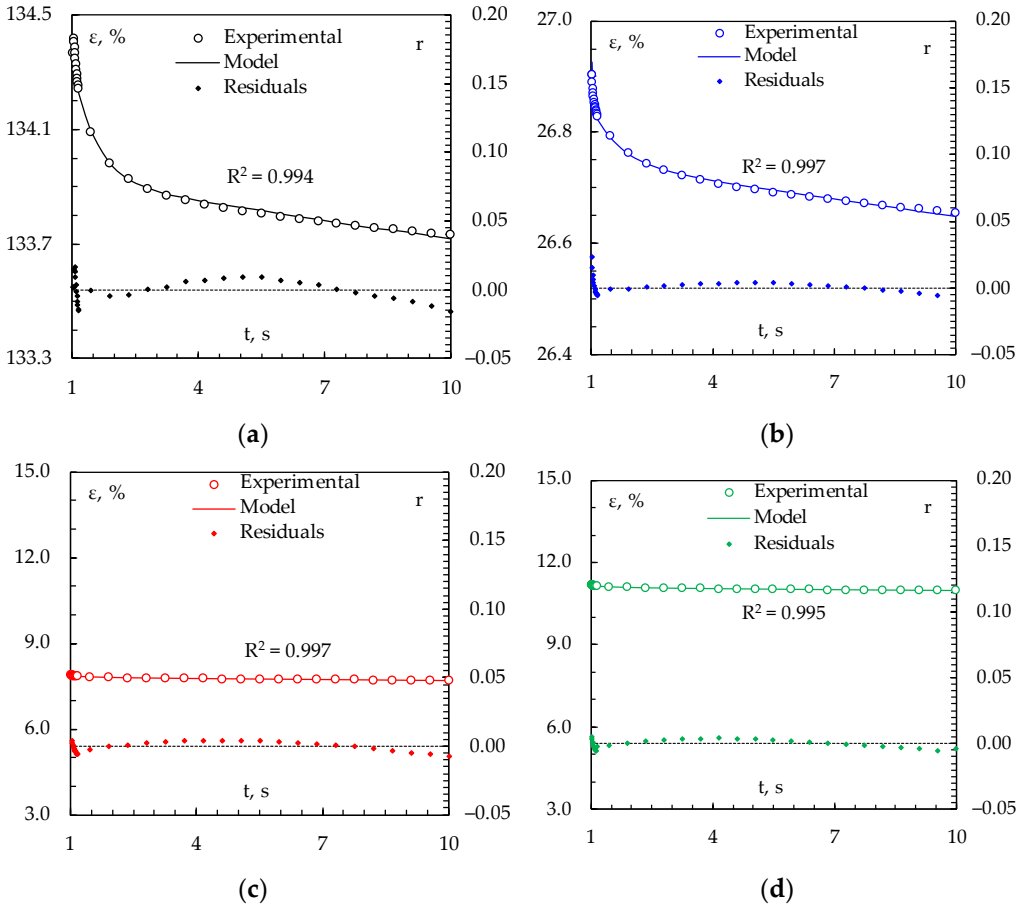

Figure 6. Fractional model (recovery phase): *BIT* (**a**), *MAS-L* (**b**), *MOR-L* (**c**) and *MOR-S* (**d**) at 60 °C, 0.1 kPa.

Table 5. Fractional model fitting coefficient for all materials and test conditions.

BIT												
T [°C]	50	50	50	60	60	60	70	70	70	80	80	80
τ [kPa]	0.1	3.2	10	0.1	3.2	10	0.1	3.2	10	0.1	3.2	10
α [-]	0.498	0.471	-	0.387	0.0001	-	0.984	0.945	-	0.999	n.a. *	-
b_1 [-]	215.2	271.2	-	104.8	0.0006	-	3.145	343.1	-	0.062	n.a. *	-
b_2 [-]	5.056	4.688	-	0.748	0.666	-	0.187	0.154	-	0.205	n.a. *	-
SSE R^2	0.999	0.998	-	0.994	0.977	-	0.990	0.826	-	0.986	n.a. *	-
MAS-L												
T [°C]	50	50	50	60	60	60	70	70	70	80	80	80
τ [kPa]	0.1	3.2	10	0.1	3.2	10	0.1	3.2	10	0.1	3.2	10
α [-]	0.784	0.536	0.414	0.688	0.203	0.188	0.951	0.617	0.0001	0.991	0.990	n.a. *
b_1 [-]	460.1	1398	2468	311.8	1026	2691	38.55	1252	0.048	4.941	70.25	n.a. *
b_2 [-]	26.68	24.73	15.96	3.768	3.748	2.285	1.005	0.9043	0.548	0.332	0.265	n.a. *
SSE R^2	0.999	0.998	0.994	0.997	0.997	0.993	0.991	0.970	0.767	0.994	0.922	n.a. *
MOR-L												
T [°C]	50	50	50	60	60	60	70	70	70	80	80	80
τ [kPa]	0.1	3.2	10	0.1	3.2	10	0.1	3.2	10	0.1	3.2	10
α [-]	0.876	0.571	0.544	0.920	0.653	0.709	0.942	0.918	0.912	0.943	0.986	n.a. *
b_1 [-]	361.3	2715	5180	120.6	2278	4971	58.34	488.5	452.3	21.29	49.11	n.a. *
b_2 [-]	63.88	57.42	42.41	9.692	11.17	7.184	2.466	2.726	0.512	0.848	0.782	n.a. *
SSE R^2	0.999	0.999	0.998	0.997	0.995	0.995	0.996	0.989	0.991	0.993	0.879	n.a. *
MOR-S												
T [°C]	50	50	50	60	60	60	70	70	70	80	80	80
τ [kPa]	0.1	3.2	10	0.1	3.2	10	0.1	3.2	10	0.1	3.2	10
α [-]	0.914	0.621	0.623	0.942	0.824	0.897	0.991	0.998	0.999	0.934	0.999	0.999
b_1 [-]	385.9	3114	6363	101.7	2771	5459	68.59	13.41	12.37	28.79	4.655	9.455
b_2 [-]	110.5	76.92	61.16	14.55	17.76	12.39	5.853	7.445	3.744	1.310	1.895	0.761
SSE R^2	0.994	0.999	0.999	0.995	0.995	0.993	0.988	0.990	0.984	0.969	0.996	0.879

* n.a.: not available for fitting inconsistency.

In general, a progressive increase of α parameters should be expected when the viscosity started to prevail (e.g., at higher test temperatures). Similarly, at fixed temperature and stress level, stiffer materials should present lower α values. In reality, such hypothetical behaviors were not clearly observed; in this regard, as reported by other researchers [36], a combined evaluation of all parameters (α, b_1, b_2) could explain this experimental finding (elasticity/viscosity predominance is affected by α but also by b_1 and b_2). In particular, the relative contribution given by the springpot to the overall deformation seemed higher than that of the dashpot. Otherwise, it is worth noting that b_1 and b_2 were sensibly reduced when increasing T, and this indicated the general weakening of material performance (i.e., higher strain accumulation as already observed by lower $R_{\%}$ and greater J_{nr}). The stress dependency was then assessed considering the coefficients of each material at fixed temperature: in this case, the decrease of α and b_2, together with the increase of b_1, illustrate behaviors reversed towards the spring case. Otherwise, it must be considered that, at high stress levels (at least higher than 0.1 kPa), secondary non-linear effects could influence the global visco-elastic response of materials [38]. Comparing *MOR-S* with *MOR-L* (reference), the inclusion of harder steel slag mainly influenced b_1 parameter related to stiffness.

Given the mathematical complexity of the proposed model, a further analysis of MSCR experimental data was performed with the objective of describing the creep-recovery phase. To this aim, two physical parameters were considered, studying the evolutive behavior of the strain during each test cycle. For the initial creep phases (1 s duration), quasi-linear time–strain relationships were identified. Therefore, for a given material, temperature, and stress, a unique average creep-slope (s) was calculated as the average of the creep slopes of each of the ten cycles. Similarly, a univocal parameter was calculated averaging the ten recovery phases (9 s duration): this was referred to as the delay (d) related to the time needed to develop an established amount of deformation within the cycle. Parameter d was thus identified as time passing from the load removal (1 s) to the beginning of a linear time-strain relationship (Figure 7). This linear recovery phase was determined by checking the gradient of punctual creep slopes below a fixed tolerance value of 0.0005 %/s. Under these assumptions, d parameter was assumed to clarify the recovery aptitude because the recovered strain was almost achieved during the delay time; after the delay time, recovered deformation was quasi-negligible. The following Figure 7 helps to clarify the physical meaning of the parameters introduced.

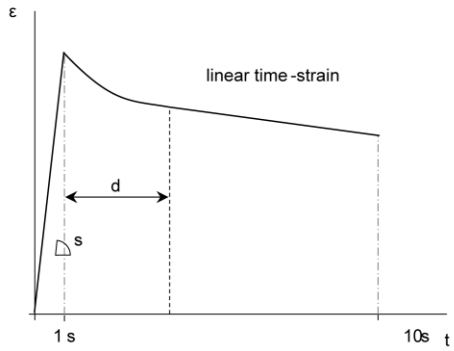

Figure 7. Physical meaning of s and d parameters for a generic creep-recovery cycle.

The calculated s and d are plotted in Figure 8 as a function of stress and temperature. Then, power and linear laws for s and d were used to reliably fit their trends over time according to Equations (6) and (7), respectively;

$$s(T) = A \cdot T^B \tag{6}$$

where, A is related to the curve position and B indicates its slope (power law coefficients).

$$d(T) = m \cdot T + q \tag{7}$$

where, m is the slope and q is the intercept of the regression line.

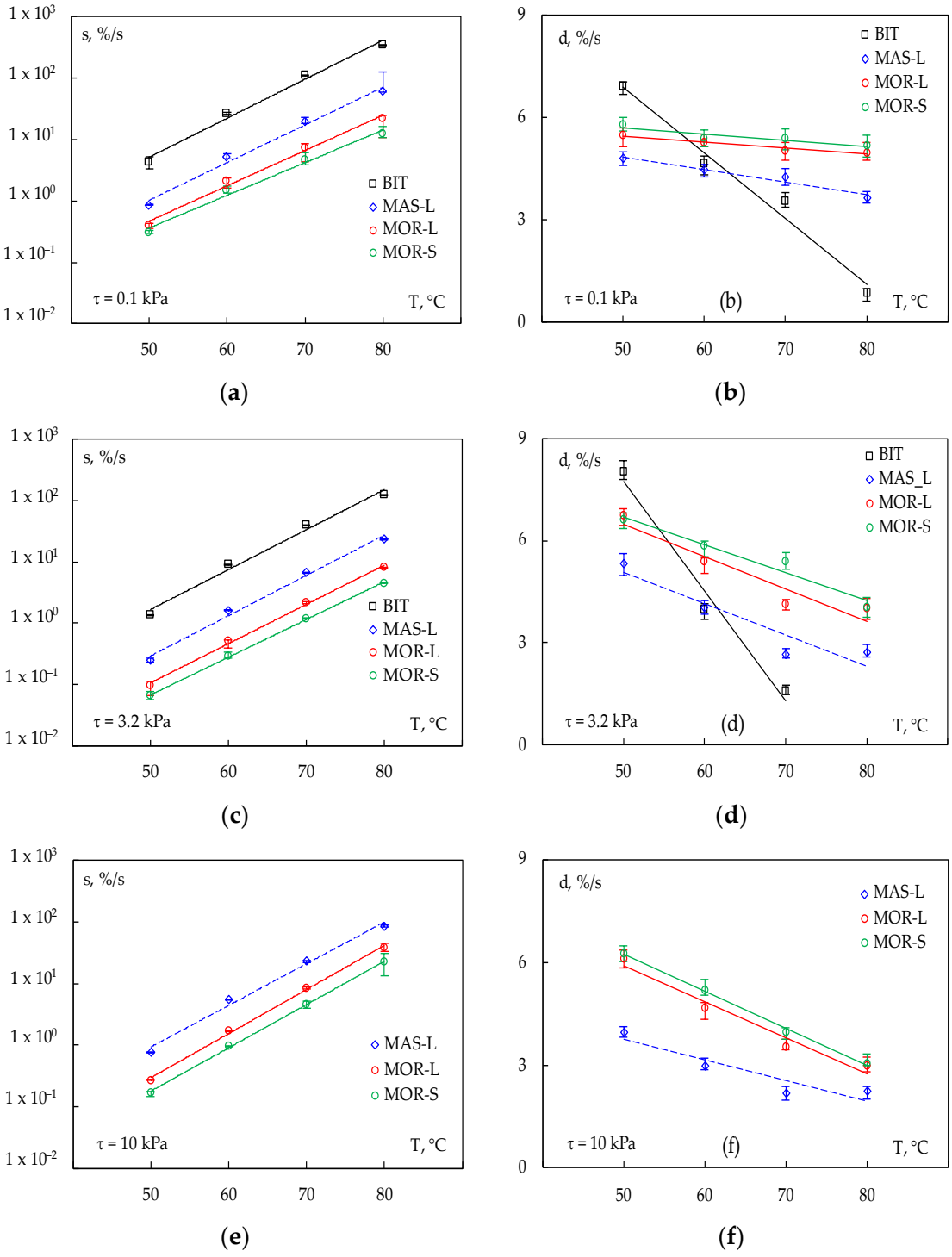

Figure 8. Physical parameters describing creep-recovery strain evolution: s (**a**) and d (**b**) at 0.1 kPa; s (**c**) and d (**d**) at 3.2 kPa; s (**e**) and d (**f**) at 10 kPa.

Table 6 reports the fitting parameter obtained for s and d evolution over time, at the different experimental temperatures and stress levels (the fitting reliability was demonstrated by high coefficients of determination R^2).

Table 6. Physical parameters describing creep-recovery strain evolution.

Material	τ [kPa]	s			d		
		A	B	R^2	m	q	R^2
BIT	0.1	0.0035	0.1461	0.9875	−0.1937	16.586	0.9775
	3.2	0.0943	0.1496	0.9869	−0.3225	23.863	0.9776
MAS-L	0.1	0.0009	0.1411	0.9886	−0.0365	6.675	0.9553
	3.2	0.0155	0.1509	0.9907	−0.092	9.6559	0.8854
	10	0.0383	0.1560	0.9910	−0.0601	6.7586	0.8569
MOR-L	0.1	0.0006	0.1324	0.9898	−0.0177	6.338	0.9524
	3.2	0.0069	0.1469	0.9973	−0.0947	11.213	0.9149
	10	0.0077	0.1651	0.9979	−0.1058	11.217	0.9675
MOR-S	0.1	0.0008	0.1224	0.9885	−0.0183	6.6292	0.8581
	3.2	0.0058	0.1413	0.9995	−0.0816	10.759	0.9529
	10	0.0055	0.1619	0.9994	−0.1087	11.698	0.9966

Generally, quasi-negligible fluctuations of 10-cycle data among the mean values were detected (see error bars in Figure 8). As far as *s* is concerned, *A* parameter (curve position) seemed to be inversely related to the material stiffness; as expected, lower creep slopes were found for the stiffer material; this means that the stiffer *MOR-S* accumulate lower creep deformation at a given T and τ with respect to other materials (lower creep slope at the fixed duration time of 1 s). On the other hand, *B* coefficient (curve slope) was quite similar for each material and stress level, suggesting a quite similar thermal and stress dependency of the creep slope. As far as the delay *d*, the slope *m* (linear interpolation) was quite different depending on material and stress level. In general, the thermal dependency was reduced (lower *m*) when the material stiffness increased; on the contrary, the increase of stress led to amplified *m*.

It is worth noting that such an approach referring to *s* and *d* parameters allowed for discriminating among the selected materials, and was generally in accordance with the main findings from the "traditional" analysis. Moreover, it provided reasonable physical meaning in describing the high-temperature material's performance. Overall outcomes clearly indicated that an increased stiffness leads to a delayed development of the strain recovery (higher *d*), which can be in turn associated with a lower non-recoverable final strain; analogously, at lower test temperatures (i.e., when a predominant elastic behavior is expected), *d* was higher; then, fewer thermal-dependent behaviors were found for mastic and mortars due to the presence of aggregates that are not thermal-dependent. Finally, the stress level also decreased the materials' thermal dependency and generally reduced the time required to develop the main part of deformation recovery.

Overall, such a comprehensive and innovative analysis of the rutting potential of fine mortars proved the suitability of steel slag in enhancing the anti-rutting properties of asphalt mixtures.

5. Conclusions

The present experimental investigation aimed at evaluating the rutting potential of different asphalt materials, which were designed based on thermal considerations only during a previous study on asphalt solar collectors. A comprehensive rheological characterization through DSR tests at the unconventional fine-mortar scale, along with an innovative modeling of the experimental data, were performed to this aim. Based on this approach, the following main findings can be summarized:

- with respect to the selected binder (plain 50/70 pen grade non-modified bitumen), the $G^*/sin\delta$ parameter indicated a PG upper limit almost equal to 52 °C, which can be considered acceptable for such a bitumen;
- the progressive inclusion of lithic fractions, passing from binder to mastic (bitumen + filler with size < 0.075 mm) and fine mortars (bitumen + filler + fine aggregates with size up to 0.18 mm), led to a clear stiffening effect and reduced rutting potential;

- the use of steel-slag fine aggregates at the fine-mortar scale led to an even higher stiffening effect with respect to conventional limestone fine sand, thus suggesting an enhanced rutting resistance;
- slag-based mortar was characterized by a reduced accumulation of high-temperature permanent strains with respect to conventional limestone-based materials, regardless of the testing conditions. Therefore, it can be asserted that the effective use of steel slags should be promoted to achieve environmental, economical, and mechanical benefits;
- the $R_{\%}$, J_{nr}, and J_{nr}/J_{tot} parameters calculated from MSCR test results were not sufficient to fully understand the rutting potential of materials, since the creep-recovery responses could be characterized by different evolutive recoverable strains after load removals;
- a fractional model, constituted by a springpot and a dashpot in series, reliably fitted the evolution of the permanent deformation not only at binder scale, but also at mastic and fine-mortar scale;
- the creep-recovery mechanisms could be also accounted for with simple physical parameters: in particular, the delay in time of the visco-elastic recovery could be a reliable index of the rutting issues, and could be also linked to the material stiffness (the higher the delay, the higher the stiffness and the related rutting resistance).

Based on the above considerations, at this research stage it can be supposed that there are no significant rutting issues for the investigated materials. Indeed, the research contributed to advancing the knowledge about the creep-recovery rheological analysis, since DSR testing can be effectively used for mastic and fine mortar characterization, even dealing with unconventional materials such as steel slag. The same concerns could be addressed regarding the fractional calculus and the analytical study of the creep-recovery phases for approximating the physical responses of such asphaltic materials.

Further studies are currently in progress to assess the rutting performance at the mixture scale, with particular attention to the role of the aggregate matrix in the development of the rutting phenomena.

Author Contributions: Conceptualization, A.B. and M.P.; methodology, A.B. and E.P.; software, A.B.; validation, G.G. and A.B.; formal analysis, E.P. and A.B.; investigation, A.B. and G.G.; resources, G.G. and A.B.; data curation, A.B. and E.P.; writing—original draft preparation, A.B. and E.P.; writing—review and editing, A.B., M.P. and G.G.; visualization, G.G.; supervision, M.P. and E.P.; project administration, M.P.; funding acquisition, M.P. All authors have read and agreed to the published version of the manuscript.

Funding: This study presents a part of the outcomes of a research project funded by the Department of Civil, Environmental and Architectural Engineering (ICEA) of the University of Padua (project n. BIRD217038/21).

Institutional Review Board Statement: Not applicable.

Informed Consent Statement: Not applicable.

Data Availability Statement: The data presented in this study are available on request from the corresponding author. The data are not publicly available because they are a part of ongoing research.

Conflicts of Interest: The authors declare no conflict of interest.

References

1. Khan, S.; Nagabhushana, M.N.; Tiwari, D.; Jain, P.K. Rutting in flexible pavement: An approach of evaluation with accelerated pavement testing facility. *Procedia Soc. Behav. Sci.* **2013**, *104*, 149–157. [CrossRef]
2. Fwa, T.F.; Pasindu, H.R.; Ong, P. Critical rut depth for pavement maintenance based on vehicle skidding and hydroplaning consideration. *J. Civ. Eng.* **2012**, *138*, 423–429. [CrossRef]
3. Nguyen, T.D.; Le, L.X. Evaluating the possible use of high modulus asphalt mixtures in flexible pavements in Vietnam. *Lect. Notes Civ. Eng.* **2020**, *80*, 701–708.
4. Qinglin, S. *Premature Damage and Its Preservative Measures of Bituminous Pavement on Expressway*; China Communications Press: Beijing, China, 2009.
5. Ali, Y.; Irfan, M.; Ahmd, S.; Ahmed, S. Empirical correlation of permanent deformation tests for evaluating the rutting response of conventional asphaltic concrete mixtures. *J. Mater. Civ. Eng.* **2017**, *29*, 04017059. [CrossRef]

6. Coleri, E.; Harvey, J.T.; Yang, K.; Boon, J.M. A micromechanical approach to investigate asphalt concrete rutting mechanisms. *Constr. Build Mater.* **2012**, *30*, 36–49. [CrossRef]
7. Coleri, E.; Harvey, J.T.; Yang, K.; Boon, J.M. Investigation of asphalt concrete rutting mechanisms by X-ray computed; tomography imaging and micromechanical finite element modeling. *Mater. Struct.* **2013**, *46*, 1027–1043. [CrossRef]
8. Li, Q.; Yang, H.; Ni, F.; Ma, X.; Luo, L. Cause analysis on permanent deformation for asphalt pavements using field cores. *Constr. Build Mater.* **2015**, *100*, 40–51. [CrossRef]
9. Su, K.; Sun, L.; Hachiya, Y.; Maekawa, R. Analysis of shear stress in asphalt pavements under actual measured tire-pavement contact pressure. In Proceedings of the 6th International Conference on Road and Airfield Pavement Technology, Sapporo, Japan, 20–23 July 2008.
10. Song, J.; Pellinen, T. Dilation behavior of hot mix asphalt under triaxial loading. *Road Mater. Pavement Des.* **2011**, *8*, 103–125.
11. Bonaquist, R.F.; Mogawer, W.S. Analysis of pavement rutting data from FHWA pavement testing facility Superpave validation study. *Transp. Res. Rec.* **1997**, *1590*, 80–88. [CrossRef]
12. Zou, G.; Xu, J.; Wu, C. Evaluation of factors that affect rutting resistance of asphalt mixes by orthogonal experiment design. *Int. J. Pavement Res. Technol.* **2017**, *10*, 282–288. [CrossRef]
13. Cheng, J.; Qian, X. Temperature-dependent viscoelastic model for asphalt concrete using discrete rheological representation. *Constr. Build Mater.* **2015**, *93*, 157–165. [CrossRef]
14. Koniditsiotis, C.; Kumar, A. Prediction of road pavement structural capacity from transverse profile shape. In Proceedings of the 6th International Conference on Managing Pavements, Brisbane, Australia, 19–24 October 2004.
15. El-Badawy, S.; Abd El-Hakim, R. *Recent Developments in Pavement Design, Modeling and Performance*; Springer: Berlin/Heidelberg, Germany, 2018.
16. Bahia, H.U.; Hanson, D.I.; Zeng, M.; Zhai, H.; Khatri, M.A.; Anderson, R.M. *Characterization of Modified Asphalt Binders in Superpave Mix Design*; Transportation Research Board: Washington, DC, USA, 2011.
17. Choi, Y.K. Visco-elastic analysis of the elastomeric binder shear resistance in relation to asphalt rutting. *Road Mater. Pavement Des.* **2011**, *12*, 767–794. [CrossRef]
18. Javilla, B.; Mo, L.; Hao, F.; An, S.; Wu, S. Systematic comparison of two-stage analytical rutting models of asphalt mixtures. *Constr. Build Mater.* **2017**, *153*, 716–727. [CrossRef]
19. Zairi, H.; Amini, A.; Goli, A.; Mirzaiyan, D. Predicting rutting performance of carbon nano tube (CNT) asphalt binders using regression models and neural networks. *Constr. Build Mater.* **2018**, *160*, 415–426. [CrossRef]
20. Abdullah, G.M.S. 3D finite element modeling to predict the foamed sulfur asphalt marl soil mixes rutting behavior. *Ain. Shams Eng. J.* **2019**, *10*, 661–668. [CrossRef]
21. Underwood, B.S.; Kim, R.Y. Experimental investigation into the multiscale behaviour of asphalt concrete. *Int. J. Pavement Eng.* **2011**, *12*, 357–370. [CrossRef]
22. Gong, X.; Romero, P.; Dong, J.; Li, Y. Investigation on the low temperature property of asphalt fine aggregate matrix and asphalt mixture including the environmental factors. *Constr. Build Mater.* **2017**, *156*, 56–62. [CrossRef]
23. Arega, A.Z.; Bhasin, A.; De Kesel, T. Influence of extended aging on the properties of asphalt composites produced using hot and warm mix methods. *Constr. Build Mater.* **2013**, *44*, 168–174. [CrossRef]
24. Kim, Y.R.; Little, D.N. *Development of Specification-Type Tests to Assess the Impact of Fine Aggregate and Mineral Filler on Fatigue Damage*; Research Report FHWA/TX-05/0-1707-10; Texas Transportation Institute: Bryan, TX, USA, 2005.
25. Pasetto, M.; Baliello, A.; Galgaro, A.; Mogentale, E.; Sandalo, A. Preliminary study of an energy harvesting system for road pavements made with marginal aggregate. *Lect. Notes Civ. Eng.* **2019**, *48*, 101–113.
26. Santillán, N.; Speranza, S.; Torrents, J.M.; Segura, I. Evaluation of conductive concrete made with steel slag aggregates. *Constr. Build Mater.* **2022**, *360*, 129515. [CrossRef]
27. Riccardi, C.; Cannone Falchetto, A.; Losa, M.; Wistuba, M. Back-calculation method for determining the maximum RAP content in Stone Matrix Asphalt mixtures with good fatigue performance based on asphalt mortar tests. *Constr. Build Mater.* **2016**, *118*, 364–372. [CrossRef]
28. Airey, G.D.; Collop, A.; Dongre, R. Linear viscoelastic limits of bituminous binders. *J. Asph. Paving Technol.* **2022**, *71*, 89–115.
29. Djurekovic, A.; Mladenovic, G. The Performance of Bitumen Mastics with the Addition of Fly Ash. In *Bituminous Mixtures and Pavements VI*, 1st ed.; CRC Press: Boca Raton, FL, USA, 2015; pp. 115–122.
30. Anderson, D.A.; Christenson, D.W.; Bahia, H.U.; Dongre, R.; Sharma, M.G.; Antle, C.E.; Button, J. Binder Characterization and Evaluation. In *Vol. 3: Physical Characterization*; Strategic Highways Research Program: Washington, DC, USA, 1994.
31. Williams, M.L.; Landel, R.F.; Ferry, J.D. The temperature dependence of relaxation mechanisms in amorphous polymers and other glass-forming liquids. *J. Am Chem. Soc.* **1955**, *77*, 3701–3707. [CrossRef]
32. Kennedy, T.W.; Huber, G.A.; Harrigan, E.T.; Cominsky, R.J.; Hughes, C.S.; Von Quintus, H.; Moulthrop, J.S. *Superior Performing Asphalt Pavements (Superpave): The Product of the SHRP Asphalt Research Program*; Strategic Highway Research Program: Washington, DC, USA, 1994.
33. Cardone, F.; Frigio, F.; Ferrotti, G.; Canestrari, F. Influence of mineral fillers on the rheological response of polymer-modified bitumens and mastics. *J. Taff. Transp. Eng.* **2015**, *2*, 373–381. [CrossRef]
34. Sapora, A.; Cornetti, P.; Carpinteri, A.; Baglieri, O.; Santagata, E. The use of fractional calculus to model the experimental creep-recovery behavior of modified bituminous binders. *Mater. Struct.* **2016**, *49*, 45–55. [CrossRef]

35. Mainardi, F. *Fractional Calculus and Waves in Linear Viscoelasticity: An Introduction to Mathematical Models*; Imperial College Press: London, UK, 2010.
36. Caputo, M.; Mainardi, F. Linear Models of Dissipation in Anelastic Solid. *La Riv. Del Nuovo Cim.* **1971**, *1*, 161–198. [CrossRef]
37. Pasetto, M.; Baliello, A.; Giacomello, G.; Pasquini, E. Sustainable solutions for road pavements: A multi-scale characterization of warm mix asphalts containing steel slags. *J. Clean Prod.* **2017**, *166*, 835–843. [CrossRef]
38. D'Angelo, J. The relationship of the MSCR test to rutting. *Road Mater. Pavement Des.* **2009**, *10*, 61–80. [CrossRef]